SUPPLEMENT TO

Elastic Plastic Self Consistent (EPSC) Modeling of San Carlos Olivine Deformed in a D-DIA Apparatus

Pamela C. Burnley and Shirin Kaboli

Detailed Methods

D-DIA apparatus. The experiments described in this manuscript were conducted using the D-DIA apparatus (Durham et al., 2002; Wang et al., 2003; Weidner and Li, 2006; Weidner et al., 2010) located at beam line 6BM-B at the Advanced Photon Source, Argonne National Laboratory. The D-DIA is a cubic multi-anvil apparatus that produces a high temperature, high pressure environment capable of controlled 'uniaxial' deformation (Durham et al., 2002; Wang et al., 2003).

Sample Assembly. The sample assembly (Figure S1) is based on the sphere-in-seats design (Durham et al., 2009); which consists of a mullite sphere with a 3mm cylindrical hole and unfired pyrophylite seats. The hole contains a thin cylindrical graphite furnace in an alumina support sleeve with a BN sleeve inside the furnace which provides confinement for the sample. The sample consisted of a pulverized polished single crystal of San Carlos olivine in series with a fully dense Al_2O_3 'inner piston' (Coors AD998) all enclosed in a 25μm thick Ni metal jacket. The Ni metal foil is required to stabilize the Fe bearing olivine and is thin enough so that it does not interfere measuring diffraction from the sample. 25μm thick Pt foils were placed at the top and bottom of the olivine specimen and the bottom of the inner piston in order to measure the length of both during the experiment. A crushable alumina piston was used to transmit the load from the bottom anvil to the sample. A W3%Re – W25%Re thermocouple inside a fully dense

Al_2O_3 insulating tubes was mounted at the top end of the sample assembly, but as described below, was not used to determine temperature. In this configuration, the thermocouple serves double duty as a piston. The thermocouple insulation consisted of a 0.03125 inch OD 4 hole Al_2O_3 tube cut at 45° assembled so as to form an elbow with the vertical portion of the insulation seated into a notched, single hole Al_2O_3 tube with a 0.0625 inch OD tube. This tube was cut slightly longer than the vertical portion of the 4 hole insulator such that the bead was essentially flush with its edge. The bead was formed by crossing the hooked the ends of the wires back into the empty channels of the vertical portion of the 4 hole insulator. The empty channels in the insulator and the space around the bead were filled with Zirconia cement (Cotronics #940).

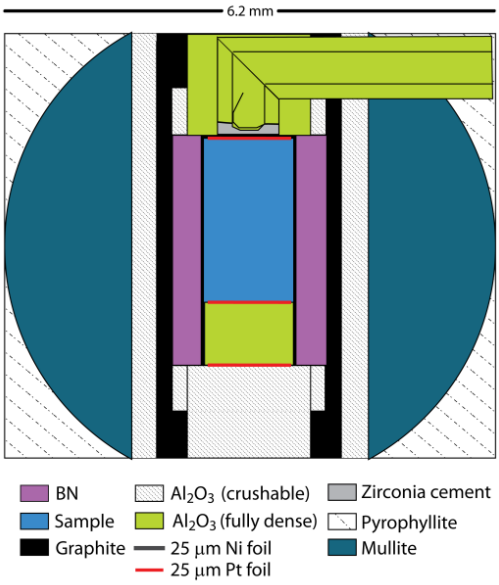

Figure S1 Schematic of the D-DIA sample assembly. The out 6.2 mm cube is of the sphere in seats design. The sample and inner alumina piston were enclosed in a 25 µm thick Ni metal jacket and surrounded by a confining medium sleeve of boron nitride (BN). Platinum (Pt) foils were placed between the sample and alumina inner piston as well at the end of the Ni capsule to function as strain markers. A top entry thermocouple was constructed of fully dense alumina insulators and sealed with Cotronics 940 ceramic cement.

Temperature Measurement. Thermocouples in D-DIA experiments are fragile and often break. In addition, the presence of the thermocouple may perturb the thermal environment around the bead. Due to high thermal gradients at the edges of the cell, we have also observed that for end-mounted thermocouples, the hotspot is at a significantly higher temperature than the thermocouple reports. We therefore have adopted a strategy of calibrating the power vs

temperature relationship for the cell design and then using the thermocouple (to the extent that it functions) to determine if the power vs thermocouple temperature relationship holds for each individual cell. The relationship between the temperature at the hotspot vs power to the sample cell was determined for this cell design based on the previously calibrated reaction kinetics of $MgO + Al_2O_3 = MgAl_2O_4$ (van Westrenen et al., 2003; Watson et al., 2002). Our temperature calibration experiments were conducted by replacing the sample with alternating plates of MgO and Al_2O_3. The calibration experiments were conducted at 3 GPa and 1430°, 1480°, and 1586° C. The widths of the $MgAl_2O_4$ reaction rind between the MgO and Al_2O_3 were measured using backscattered electron (BSE) micrographs in the scanning electron microscope (SEM). The thickest rinds occurred in the middle portion of the sample and the widths of these rinds, combined with the known length of the time at temperature, were used to calculate the temperature of the hotspot. The difference between the temperature at the hotspot and that recorded by the thermocouples was consistent with thermal models of the sample assembly calculated using CellAssembly (Hernlund et al., 2006). The maximum difference between a linear best fit of furnace power versus hot spot temperature and the measured hot spot temperature was ~3% of the temperature.

For this experiment, the thermocouple worked during initial heating up to 700 C and then failed. The thermocouple temperature vs power for the cell was consistent with those measured during the calibration experiments so the power vs temperature relationship from the calibration experiments was used to determine the hotspot temperature.

Experimental Procedure. The experiment was compressed at room temperature to ~ 6 GPa (as estimated by diffraction from the olivine). Then the temperature was raised to 1200 C and the

sample annealed for 3 hours and 50 minutes. The temperature was then lowered to the first experimental temperature. X-ray spectra were collected at this initial condition and then the D-DIA inner rams were advanced to deform the specimen while in-situ diffraction observations were made. The motor speed for the D-DIA ram pumps was chosen to produce a strain rate of ~ $5x10^{-6}$/sec, a strain rate which would allow better documentation of the low strain behavior of the sample. After 3 - 4% strain was achieved, the motors for the inner rams were stopped. The temperature was then raised to 1200 C and the inner rams were retracted briefly at rate ~10^{-5}/sec to relax any remaining stresses. This sequence of short deformation experiments and relaxation periods was repeated for the four temperature conditions reported here. No effort was made to adjust the experimental pressure beyond the automatic feedback system that keeps the oil pressure constant. Thus, the pressure for each deformation was slightly different.

Pressure evolution during the experiment. During this initial heating and annealing phase, the cell material extrudes and stresses within the assembly relax. This results in a substantial loss of pressure, especially for this particular cell assembly. When the temperature is subsequently lowered, the cell pressure drops further due to thermal contraction. The effect of thermal contraction and expansion on pressure can be seen in Table 1; the pressure for each deformation sequence is higher as the temperature is increased. We did not attempt to adjust the pressure between deformation sequences because of the inherent risks of doing so.

In-situ X-ray measurements. The design of the D-DIA allows the synchrotron x-ray beam to enter the sample assembly via the gap between the side anvils. A sintered diamond transparent anvil is used on the downstream side to allow the diffracted x-rays to be observed by an array of energy dispersive detectors. A conical slit, which sits up-stream of the detectors, determines the

two theta angle of the diffracted x-rays and eliminates diffraction from the sample assembly (Weidner et al., 2010). Because the x-ray source is white, each detector measures a full powder pattern from the sample. We refer to diffraction collected from the detectors for which ψ=0° and 180° (see Figure S2) as being measured in the compression direction and diffraction measured with ψ= 90° and 270° degrees as being measured in the transverse direction.

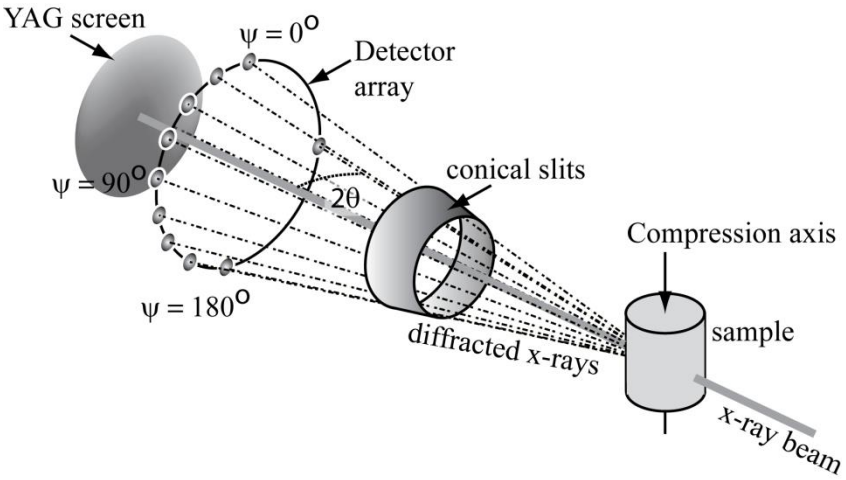

Figure S2: Diffraction geometry for D-DIA experiments. For clarity, the apparatus is not shown but the direction of the compression axis and the sample are shown along with the orientation of the incoming x-ray beam, the position of the ten detectors and the YAG screen. The conical slit is shown schematically.

Lattice spacings were derived from the diffraction patterns via calibration spectra that were collected at the start of the experiment. All spectra were collected for a duration of 60 seconds and then manually summed with other spectra in order to obtain longer acquisition periods. For the calibration standard, 20 spectra were collected and summed. For sample spectra, 5 spectra were collected and summed. This system allows for analysis of peak shifts that occur within the typical 300 second collection time. It also avoids any possible intensity based shifts originating from the detector electronics when comparing spectra collected over different periods of time. During the deformation portions of the experiment, alternating sets of radiographs and 5 60-

second spectra from the sample, and the alumina inner piston were taken. During diffraction acquisition the press was moved vertically in ~20 micron increments from one end of the sample to the other in order to increase the effective diffraction volume from the sample. The portion of the sample within 150 microns of the end was not measured during the scan to avoid shadowing effects from the Pt foils. This vertical scanning procedure was also used to collect diffraction from the inner piston. Strain in the sample was measured by comparing the length of the sample in radiographic images made from the transmitted x-ray beam (Vaughan et al., 2000) as recorded by a fluorescent YAG screen located at the center of the conical slit (See figure S2). The radiographic images were analyzed using Image-J (Schneider et al., 2012). The starting length of the sample l_0 was recorded at the pressure and temperature conditions of the experiment immediately before the D-DIA rams begun advancing for each deformation sequence. Sample strain is calculated as $\epsilon = {(l - l_0)}/{l_0}$ where l is the instantaneous sample length. Sample strain measurements are not synchronous with the diffraction measurements; therefore, the sample strain associated with each diffraction measurement must be calculated. Since we typically observe some sluggishness in the system when deformation first begins, rather than calculating sample strain from a linear fit all the sample strain vs time data, we fit the data with a polynomial function (Figure S3). This is particularly important for characterizing the slope of the stress strain curve at the lowest strains. Quoted strain rates (Table 1) are for the portion of the experiment after the sample strain vs time behavior becomes linear.

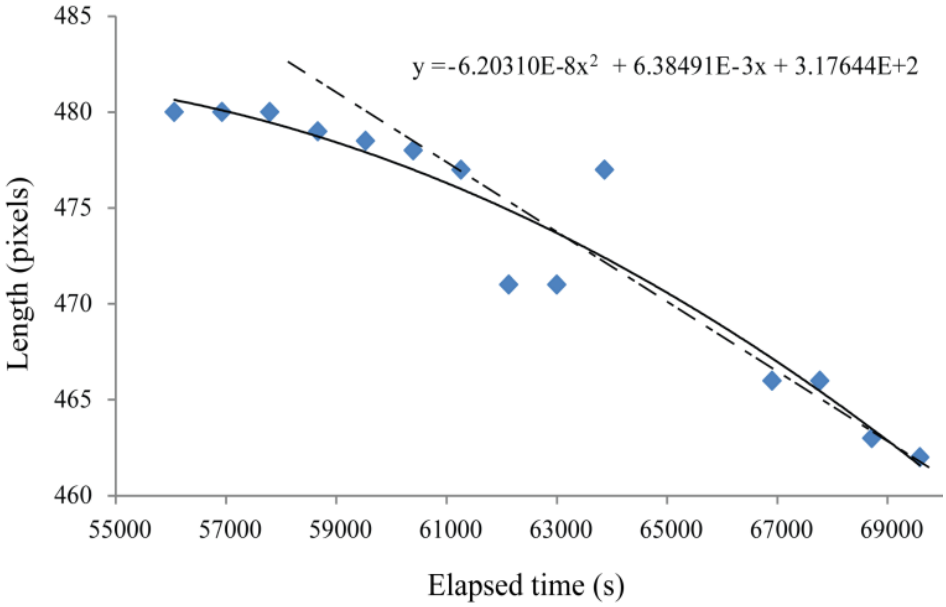

Figure S3: Plot of sample length in pixels as a function of elapsed time for the second deformation sequence. The initial strain rate is slower than later in the experiment. To calculate the sample length that correlates with each diffraction measurement, a polynomial function (solid line) is used rather than a linear fit. The dashed line shows the linear fit used to estimate the overall strain rate.

X-ray diffraction data analysis

The position of x-ray diffraction peaks as a function of time and ultimately sample strain is determined by fitting each peak of interest in each spectra with the program Plot85, which uses a pseudo-Voigt peak-fitting routine (Figure S4). For San Carlos olivine, the (130), (131), (112), (122), (140), and (211) diffraction peaks were analyzed. Before peak-fitting of the spectra, a background correction was performed by subtracting spectra collected from a sample assembly which contained a furnace and BN sleeve but did not contain a sample or Ni capsule.

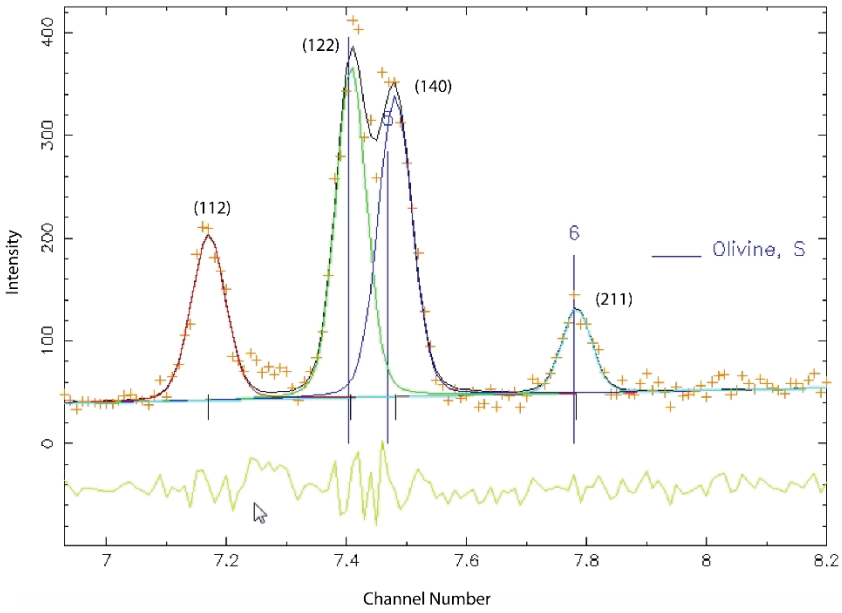

Figure S4: Example of peak fits of x-ray spectra in Plot85 for the (112), (122), (140) and (211) peaks. The crosses are data points. Individual peak fits (colored lines) are shown as well as their sum (black line). The difference between the peak fit and the raw data points is plotted in green at the bottom of the plot. Channel number is converted to d-spacing in Angstroms via calibration coefficients.

Lattice strain (ε^{hkl}) is calculated independently for each deformation sequence as follows:

$$\varepsilon^{hkl} = \frac{\left(d^{hkl} - d_0^{hkl}\right)}{d_0^{hkl}}$$

where d_0^{hkl} is the lattice spacing measured by a given detector at the point at which the sample is experiencing a hydrostatic condition. In most cases this is immediately before the beginning of deformation for each sequence. On some occasions the sample is under relative tension (the transverse lattice spacings are smaller than those measured in the compression direction) because of differences in the thermal contraction of the sample assembly parts. In this circumstance d_0^{hkl} is taken as the lattice spacing when the sample reaches a hydrostatic condition as it transitions from relative tension to compression. Since the 5 60 second spectra are collected over an extended period (typically 310 seconds) the mid-point time is used for the correlation with

sample strain data. The midpoint time is calculated as the time halfway between 60 seconds prior to the time stamp on the first of the set of 5 diffraction patterns and the time stamp on the last of the 5 diffraction patterns.

EPSC Models

In order to interpret the diffraction measurements, lattice strain vs sample strain curves for the experiments are compared with simulated diffraction data generated with an elastic plastic self-consistent (EPSC) model. An EPSC code (EPSC3) provided by C. N. Tome (Tome and Oliver, 2002) was used; with some minor modifications as discussed in (Burnley, 2015). For the grain orientation input file we used 49,108 grains that were distributed through Euler space by incrementing each Euler angle by 5 degrees (Burnley, 2015). Unit cell dimensions and single crystal elastic constants for the EPSC models were calculated for the pressure temperature conditions appropriate to each deformation sequence and are given in Table S1.

Table S1 – unit cell parameters used in EPSC models

T °C	P (GPa)	a (Å)	b (Å)	c (Å)
440	3.8	4.744	10.144	5.965
663	4.3	4.752	10.170	5.973
882	4.5	4.760	10.196	5.991
1106	4.6	4.770	10.232	6.009

The pressure for each experiment was calculated from the diffraction from the olivine collected immediately before the deformation step was initiated, using a second order Birch–Murnaghan isothermal equation of state (Birch, 1947). The bulk modulus from (Knittle, 1995) and thermal expansion coefficients from (Fei, 1995) were used. The Cij for each deformation sequence were calculated for the appropriate temperature and pressure using constants from

(Isaak, 1992), (Anderson and Isaak, 1995). (Abramson et al., 1997) (Liu and Li, 2006) and are listed in Table S2.

Table S2 – Single crystal elastic constants in GPa used in EPSC models

T C	P (GPa)	C_{11}	C_{22}	C_{33}	C_{44}	C_{55}	C_{66}	C_{12}	C_{13}	C_{23}
440	3.8	331.3	202.1	236.9	65.7	77.7	79.9	72.79	76.7	78.3
663	4.3	321.3	196.0	229.4	62.5	74.0	76.3	71.19	75.8	77.4
882	4.5	308.7	188.6	220.1	59.1	70.2	72.3	68.63	73.6	75.6
1106	4.6	294.4	180.5	209.6	55.4	66.1	67.9	65.64	71.0	73.4

EPSC simulations were run with a uniaxial strain boundary condition and compressive strain was used as the control variable. Strain in the transverse directions as well as all stresses were allowed to vary freely. Changes in confining pressure during compression were not included in the models, which is appropriate because the pressure did not increase significantly during each deformation sequence. Models were run to a maximum of 4% compressive strain calculated over 500 displacement increments. We model the eight commonly observed slip systems in olivine as well as three unidirectional slip systems to simulate the formation of kink bands (Burnley, 2015; Kaboli et al., 2017). For this study we also used an additional isotropic deformation mechanism which consisted of 30 slip planes (Table S3). We used the open source program VESTA (Momma and Izumi, 2011) to visualize which planes would be most useful for the model.

Table S3 – planes used in isotropic slip system

$(\bar{1}11)[23\bar{1}]$, $(\bar{1}11)[101]$, $(\bar{1}11)[0\bar{1}1]$
$(111)[2\bar{3}1]$, $(111)[10\bar{1}]$, $(111)[0\bar{1}1]$
$(1\bar{1}1)[231]$, $(1\bar{1}1)[\bar{1}01]$, $(1\bar{1}1)[011]$
$(1\bar{1}\bar{1})[23\bar{1}]$, $(1\bar{1}\bar{1})[101]$, $(1\bar{1}\bar{1})[0\bar{1}1]$
$(120)[2\bar{1}0]$, $(\bar{1}20)[210]$
$(301)[\bar{1}03]$, $(30\bar{1})[103]$
$(021)[11\bar{2}]$, $(021)[\bar{2}1\bar{2}]$, $(021)[01\bar{2}]$
$(02\bar{1})[1\bar{1}\bar{2}]$, $(02\bar{1})[212]$, $(02\bar{1})[0\bar{1}\bar{2}]$
$(2\bar{3}1)[431]$, $(23\bar{1})[\bar{4}31]$, $(\bar{2}31)[\bar{4}\bar{3}1]$, $(231)[\bar{4}3\bar{1}]$
$(2\bar{3}1)[124]$, $(23\bar{1})[\bar{1}24]$, $(\bar{2}31)[\bar{1}\bar{2}4]$, $(231)[\bar{1}2\bar{4}]$

The EPSC model uses a Voce hardening law to describe the evolution of the critical resolved shear stress (τ) with shear strain (Γ) as follows:

$$\tau = \tau_0 + (\tau_1 + \phi_1\Gamma)\left[1 - e^{-\left(\phi_0\Gamma/\tau_1\right)}\right]$$

where τ_0 is the initial critical resolved shear stress and τ_1, ϕ_0, and ϕ_{01} are parameters that control the rate of hardening after the CRSS is reached (Turner and Tome, 1994). The critical resolved shear stress and hardening parameters for the slip and kink systems were adjusted so that the numerical diffraction data from EPSC models closely matched the experimental diffraction data from the D-DIA experiments. The value of τ_0, τ_1, ϕ_0, and ϕ_1 used in each model are listed in Table 2 in the main manuscript.

When comparing the EPSC models with our diffraction data, we only use diffraction from the compression (ψ = 0° and 180°) and transverse (ψ = 90°) detectors. As described in (Burnley and Zhang, 2008), the only detectors positioned such that all grains contributing to any

given single diffraction peak have the same Schmid factor are those at ψ = 0° and 180° (the compression direction). For the other detectors, the grain populations contributing to each diffraction peak have a wide range of Schmid factors and therefore are experiencing different degrees of plastic deformation.

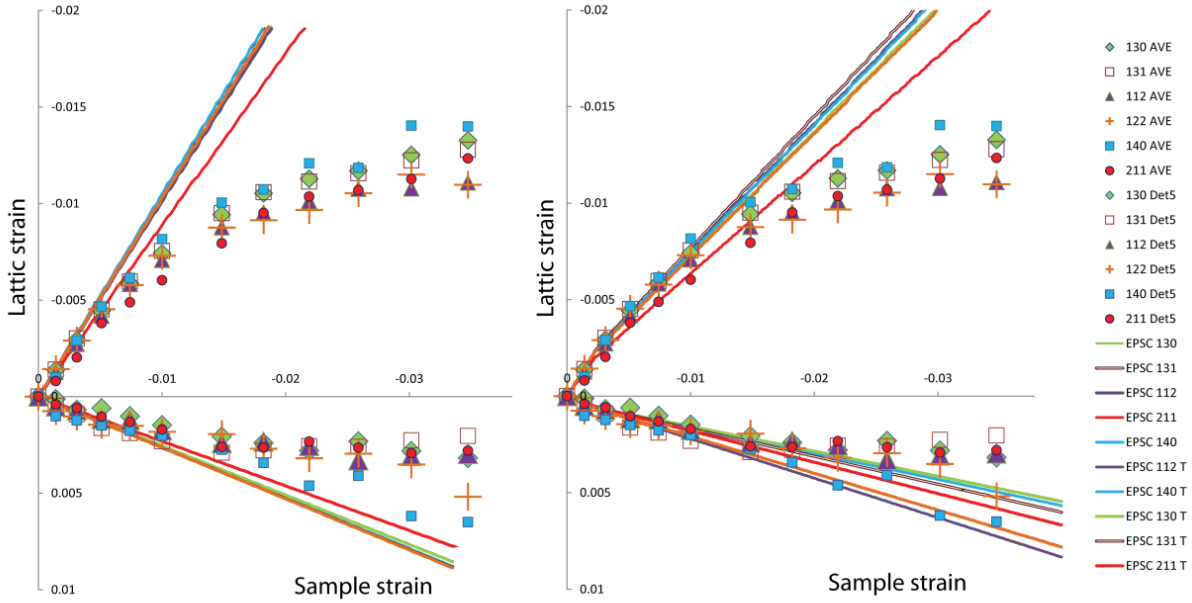

Figure S5: Comparison between purely elastic EPSC model (left) and EPSC model which includes the isotropic system (right) for the first deformation sequence (440C, 3.8 GPa). The CRSS and hardening parameters used for the isotropic system are $\tau_0 = 0.2$, $\tau_1 = \phi_0 = \phi_1 = 60$. The transition between the pure elastic behavior and the isotropic behavior can be seen between the origin and the first group of data points (right). Note that the degree of spreading between lattice strains is very similar between the two models. The data points are from the diffraction experiment.

The EPSC model takes this into account. However, in practice, the limited number of grains in the diffracting volume can produce substantial scatter in the diffraction data which in turn puts fewer constraints on the EPSC model parameters. Thus, we focus the majority of our attention in fitting the models to the compression detectors and use the transverse detector data to

monitor overall pressure changes. The diffraction data from the other detectors should give lattice strains that are intermediate between those of the compression and transverse detectors. Thus, these detectors are used as a check on data quality.

Sample Description

After the experiment, the olivine sample was examined by Electron Backscatter diffraction. Mapping was carried out at a 70 degree specimen tilt with a Nordlys II system using a Hitachi SU-8000 cold-field emission scanning electron microscope (CFE-SEM) at a 20 keV electron beam energy and a 19.4 mm WD. Indexation and analysis of maps were performed using HKL Channel 5 Flamenco software. Sample preparation was similar to that described in (Kaboli et al., 2017) for forsterite olivine. The sample microstructure reflects all five deformation cycles, including the last one at 1200 C (the results of this cycle were not analyzed due to a failure to reach hydrostatic conditions at the beginning of deformation). The sample has a bimodal grain size (Figure S6), with the small grains probably originating from recrystallization of the original larger grains. The large grains (60% of the sample) have an average size of 35.2 μm with a standard deviation of 15.5 μm and the small grains (40%) have an average size of 3.1 μm with a standard deviation of 1.2 μm. The grain size was measured using the line intercept method (Vander Voort, 1984) and the ImageJ (Schneider et al., 2012) open-source software. The grain orientation data was divided into two subset, large grains and small grains (Figure S7). Neither grain set shows a marked preferred orientation, but internal deformation within the large grains can be inferred from the smearing of the orientations in the pole figure.

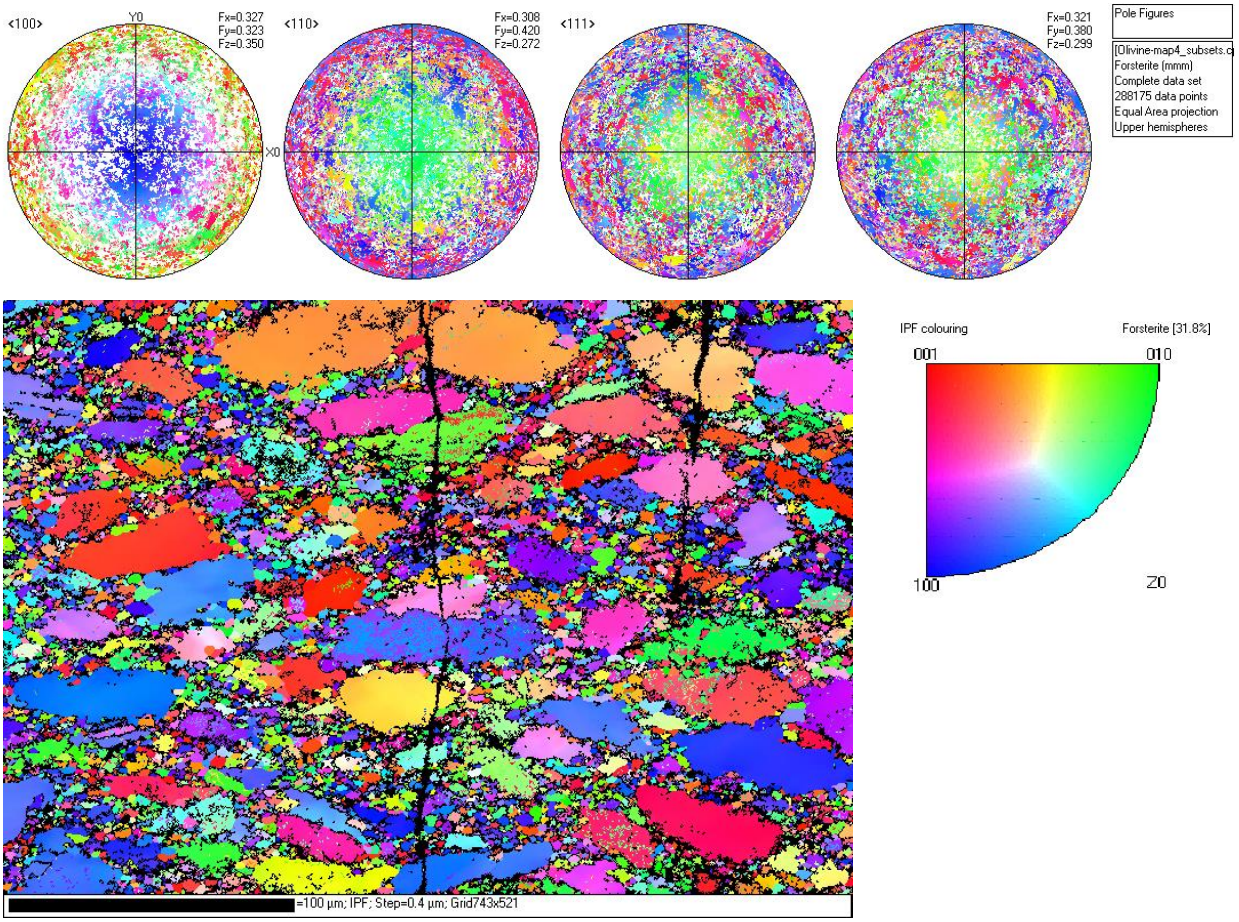

Figure S6: EBSD crystallographic orientation map and pole figures of sample after the deformation experiment. Colors in the map are tied to the inverse pole figure. The sample has a bimodal grain size. We interpret the smaller grains to have formed by recrystallization during high temperature deformation. We interpret the larger grains to be deformed remnants of the original grain population in the specimen.

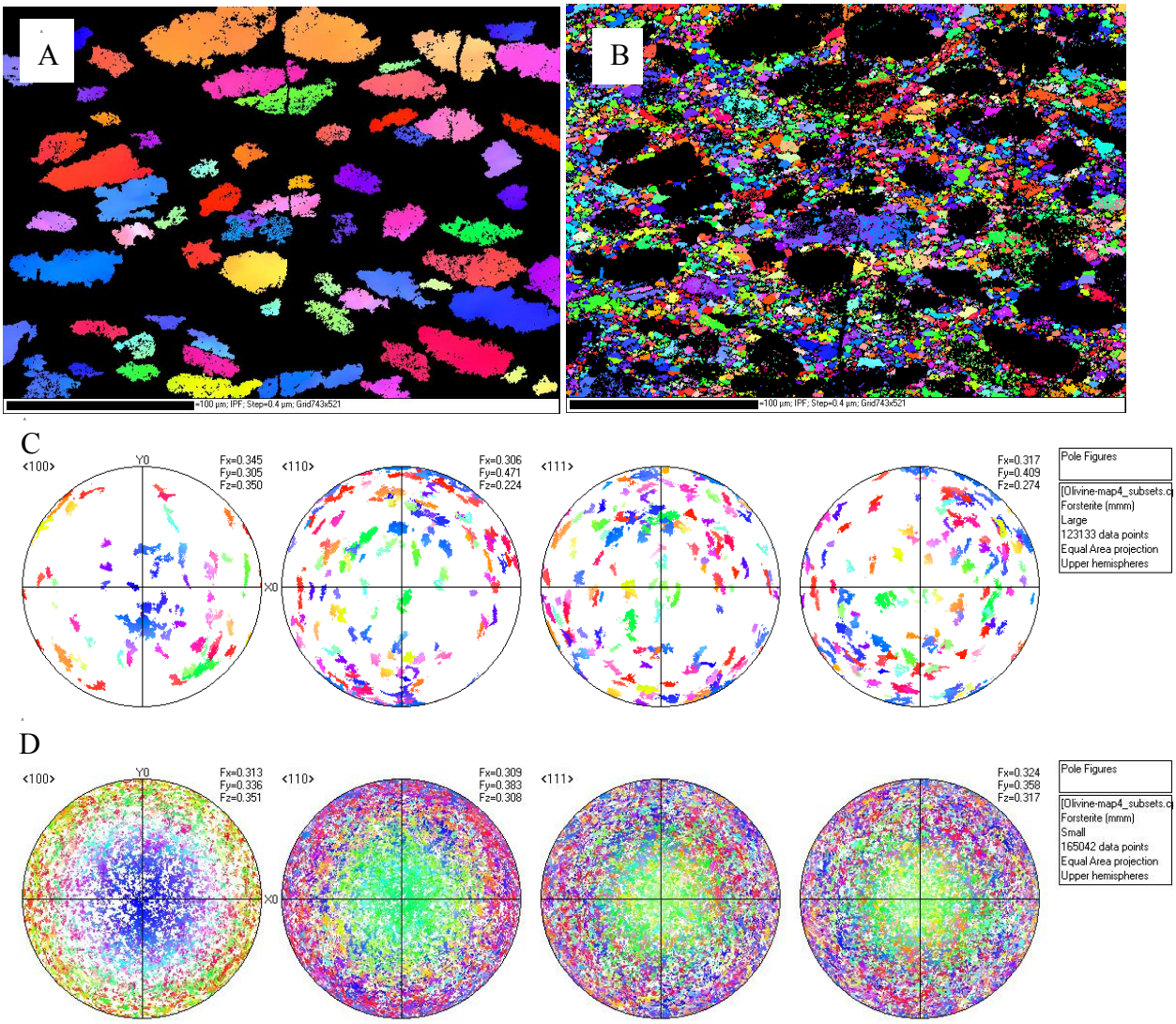

Figure S7: EBSD crystallographic orientation maps of large grains (A) and small grains (B) and pole figures of large grains (C) and small grains (D). Colors are keyed to the inverse pole figure in Figure S6. Neither grain population shows a marked preferred orientation. Deformation within the large grains can be observed in the smearing of grain orientations

References

Abramson, E. H., Brown, J. M., Slutsky, L. J., and Zaug, J., 1997, The elastic constants of San Carlos olivine to 17 GPa: J. Geophys. Res., v. 102, no. B6, p. 12253–12263.

Anderson, O. L., and Isaak, D. G., 1995, Elastic constants of mantle minerals at high temperatures, *in* Ahrens, T. J., ed., Mineral Physics and Crystallography: A Handbook of Physical Constants (Reference Shelf 2): Washington, DC, American Geophysical Union p. 64–97.

Birch, F., 1947, Finite elastic strain of cubic crystals: Physical Review, v. 71, no. 11, p. 809-824.
Burnley, P. C., 2015, Modeling of Plastic Deformation in Fayalite Olivine: American Mineralogist, v. 100, p. 1424-1433.
Burnley, P. C., and Zhang, D., 2008, Interpreting in situ x-ray diffraction data from high pressure deformation experiments using elastic-plastic self-consistent models: an example using quartz: Journal of Physics-Condensed Matter, v. 20, no. 28, p. 10 pp.
Durham, W. B., Mei, S., Kohlstedt, D. L., Wang, L., and Dixon, N. A., 2009, New measurements of activation volume in olivine under anhydrous conditions: Physics of the Earth and Planetary Interiors, v. 172, no. 1-2, p. 67-73.
Durham, W. B., Weidner, D. J., Karato, S. I., and Wang, Y. B., 2002, New developments in deformation experiments at high pressure, *in* Karato, S., and Wenk, H. R., eds., Plastic Deformation of Minerals and Rocks, Volume 51, p. 21-49.
Fei, Y. W., 1995, Thermal Expansion, *in* Ahrens, T. J., ed., Mineral Physics & Crystallography: A Handbook of Physical Constants AGU Reference Shelf, Volume 2: Washington, D.C., American Geophysical Union, p. 29-44.
Hernlund, J., Leinenweber, K., Locke, D., and Tyburczy, J. A., 2006, A numerical model for steady-state temperature distributions in solid-medium high-pressure cell assemblies: American Mineralogist, v. 91, no. 2-3, p. 295-305.
Isaak, D. G., 1992, High-temperature elasticity of iron-bearing olivines: J. Geophys. Res., v. 97(B2), p. 1871–1885.
Kaboli, S., Burnley, P. C., Xia, G., and Green, H. W. I., 2017, Pressure dependence of creep in forsterite olivine: comparison of measurements from the D-DIA and Griggs apparatus. https://doi.org/10.1002/2017GL075177: Geophysical Research Letters, v. 44, p. 10,939–910,947.
Knittle, E., 1995, Static Compression Measurements of Equations of State, *in* Ahrens, T. J., ed., Mineral Physics & Crystallography: A Handbook of Physical Constants, AGU Reference Shelf Volume 2: Washington, USA, American Geophysical Union, p. 98-142.
Liu, W., and Li, B., 2006, Thermal equation of state of $(Mg0.9Fe0.1)_2SiO_4$ olivine: Physics of the Earth and Planetary Interiors, v. 157, no. 3, p. 188-195.
Momma, K., and Izumi, F., 2011, VESTA 3 for three-dimensional visualization of crystal, volumetric and morphology data: J. Appl. Crystallogr., v. 44, p. 1272-1276.
Schneider, C. A., Rasband, W. S., and Eliceiri, K. W., 2012, NIH Image to ImageJ: 25 years of image analysis: Nature Methods, v. 9, p. 671-675.
Tome, C. N., and Oliver, E. C., 2002, Code Elastio-plastic self-consistent (EPSC): Los Alamos National Laboratory, USA.
van Westrenen, W., Van Orman, J. A., Watson, H., Fei, Y. W., and Watson, E. B., 2003, Assessment of temperature gradients in multianvil assemblies using spinel layer growth kinetics: Geochemistry Geophysics Geosystems, v. 4, no. 4, p. 10 pp.
Vander Voort, G. F., 1984, Metallography, Principles and Practice., New York, McGraw-Hill.
Vaughan, M., Chen, J., Li, L., Weidner, D. J., and Li, B., 2000, Use of X-ray imaging techniques at high pressure and high temperature for strain measurements

in Manghnani, M. H., Nellis, W. J., and Nicol, M. F., eds., Science and Technology of High Pressure Proceedings of AIRAPT-17, Universities Press, p. 1097-1098
Wang, Y. B., Durham, W. B., Getting, I. C., and Weidner, D. J., 2003, The deformation-DIA: A new apparatus for high temperature triaxial deformation to pressures up to 15 GPa: Review of Scientific Instruments, v. 74, no. 6, p. 3002-3011.

Watson, E. B., Wark, D. A., Price, J. D., and Van Orman, J. A., 2002, Mapping the thermal structure of solid-media pressure assemblies: Contributions to Mineralogy and Petrology, v. 142, no. 6, p. 640-652.

Weidner, D. J., and Li, L., 2006, Measurement of stress using synchrotron x-rays: Journal of Physics-Condensed Matter, v. 18, no. 25, p. S1061-S1067.

Weidner, D. J., Vaughan, M. T., Wang, L. P., Long, H. B., Li, L., Dixon, N. A., and Durham, W. B., 2010, Precise stress measurements with white synchrotron x rays: Review of Scientific Instruments, v. 81, no. 1, p. 5 pp.